

Interatomic force constants including the DFT-D dispersion contribution

Benoit Van Troeye,^{1,*} Marc Torrent,² and Xavier Gonze¹

¹*Institute for Condensed Matter and Nanosciences, European Theoretical Spectroscopy Facility, Université catholique de Louvain, Chemin des étoiles 8, B-1348 Louvain-la-Neuve, Belgium*

²*CEA, DAM, DIF, F-91297 Arpajon, France*

(Received 21 December 2015; published 20 April 2016)

Grimme's DFT-D dispersion contribution to interatomic forces constants, required for the computation of the phonon band structures in density-functional perturbation theory, has been derived analytically. The implementation has then been validated with respect to frozen phonons, and applied on materials where weak cohesive forces play a major role, i.e., argon, graphite, benzene, etc. We show that these dispersive contributions have to be considered to properly reproduce the experimental vibrational properties of these materials, although the lattice parameter change, coming from the ground-state relaxation with the proper functional, induces the most important change with respect to a treatment without dispersion corrections. In the current implementation, the contribution of these dispersion corrections to the dynamical matrices (with a number of elements that is proportional to the square of the number of atoms) has only a cubic scaling with the number of atoms. In practice, the overload with respect to density-functional calculations is small, making this methodology promising to study vibrational properties of large dispersive systems.

DOI: [10.1103/PhysRevB.93.144304](https://doi.org/10.1103/PhysRevB.93.144304)

I. INTRODUCTION

It is now commonly accepted that the most popular exchange-correlation energy functionals—i.e., LDA, GGA, mGGA, or hybrid functionals—fail to properly describe nonlocal dispersion effects in density-functional theory (DFT) [1]. These effects play a major role in layered materials and molecular crystals, leading to the inaccurate description of these materials by the above-mentioned functionals [2].

To overcome this difficulty, several methods have been developed over the past years. On the one hand, one finds density-dependent methods or even wave-function-dependent methods, whose implementation cost might be significant. In this category, several methods have found widespread use, like the Tkatchenko-Scheffler van der Waals (TS-vdW) corrections [3], which adds to the DFT result a term depending both on the geometry of the system and on the electronic density, or the vdW-DF methods [4–6], which add to the exchange-correlation a nonlocal term to treat the dispersive effects. The Silvestrelli approaches (vdW-WF) [7,8] use maximally localized Wannier functions to estimate the vdW correction to the Kohn-Sham (KS) energy. The random phase approximation [9–11] has also shown encouraging results in taking into account these interactions, although it still suffers from a large computational time overhead [12].

On the other hand, there are simpler, density-independent dispersion corrections that include Grimme's DFT-D methods, have been developed, with a quite significant impact as well [13–15]. In this case, the correction only depends on the nuclei positions and on the approximation for the exchange-correlation functional in use.

In DFT-D2 [13], a simple pairwise term is added to the DFT energy. It exhibits a long-range behavior $C_{6,ij}/R_{ij}^6$ where $C_{6,ij}$ is the dispersion coefficient and R_{ij} is the distance between the atoms. Although yielding better agreement with the

experiments than DFT for most noncovalently bound systems, this method only considers one coefficient for each chemical pair and thus may not be able to catch the fundamental trends of these interactions. For example, the dispersion coefficient can vary by a factor of two in the case of armchair carbon nanotubes depending of their size [16].

In the more sophisticated DFT-D3 [14], the problem is tackled with the use of environment-dependent dispersion coefficients. These coefficients are interpolated on tabulated supporting points, which have been computed beforehand in TDDFT. A three-body term—also referred as the Axilrod-Teller-Muto nonadditive term [17,18]—can also be taken into account. Finally, DFT-D3 with Becke-Johnson damping—DFT-D3(BJ) [15]—is a variant of the previously introduced DFT-D3 method that uses another expression for the damping that removes the undesired short-range divergent behavior of the correction.

In all these cases, these corrections have to be taken into account in the computation of atomic derivative-related quantities like forces, stresses, interatomic force constants (IFCs), dynamical matrices, or elastic tensors. At variance with vdW-DF or TS-vdW methods, the DFT-D ones do not lead to direct modifications of properties related to the electric field derivatives, i.e., Born effective charges, dielectric tensor or electron-phonon coupling matrix elements, as these corrections are independent of the density, except for the indirect dependence through modification of atomic positions. This is both an advantage and a drawback of these methods, as on the one hand the complexity of the equations and their implementation remains quite low but on the other hand, some effects could be lost by neglecting the density dependence of the vdW corrections.

Although it is possible to compute all the previously introduced global quantities in the case of DFT with finite difference techniques, the computations can become quite demanding, especially for dynamical matrices at small wave vectors, which require the use of large supercells. A more elegant way to calculate these quantities is achieved in density-functional

*benoit.vantroeye@uclouvain.be

perturbation theory (DFPT) [19–22], which benefits from lower computation time and more easily achieved precision. This formalism has also been extended to strain perturbations [23,24] for the computation of relaxed elastic, piezoelectric, and internal strain coupling parameters.

In this paper, we will show how the DFT-D pairwise contribution to the Fourier transform of the IFCs at any wave vector of the reciprocal space, required for the computation of the phonons frequencies and eigendisplacements, can be derived in a similar scheme. We will neglect the effect of the three-body term, as discussed later. We are aware of the existence of a DFPT phonon implementation with the vdW-DF methodology [25], although it has not been released to our knowledge. The DFT-D2 contributions to the IFCs have also been reported in the GULP software [26,27]. Except for these implementations and the related publications, the literature reports some frozen-phonon computations with dispersion corrections in periodic systems [28–32]. Our method will be afterwards applied to three materials incorrectly described by DFT in GGA, i.e., argon, graphite, and benzene.

It has to be reminded that phonon modes are quite sensitive to the geometry of the system. As these DFT-D corrections play an important role for the ground-state geometry, two effects on the phonons have to be distinguished when the vdW corrections are taken into account: an indirect effect, related to the change of geometry of the ground state, and a direct effect, which is related to the contribution of these corrections to the IFCs. It will be shown that although the largest effect of DFT-D methods on the phonon frequencies originates from geometrical modifications, the dispersion corrections to the IFCs cannot be neglected.

In Sec. II, the theoretical background will be presented, with some detailed derivations in the supplementary information. The DFT-D contribution to the dynamical matrix can be implemented with an $O(N_{\text{at}}^3)$ scaling. Taking into account the prefactor of the calculation, and the normal cost and scaling of usual DFPT calculations of a dynamical matrix, the associated computational overhead is negligible, whatever the size of the system. We will also discuss briefly in Sec. III the implementation and show that an excellent agreement can be obtained between our implementation and frozen-phonon calculations. Finally, in Sec. IV, we will present the results obtained with our implementation on specific materials.

II. THEORY

In all DFT-D methods, a density-independent pairwise contribution $E_{\text{disp}}^{(2)}$ is added to the DFT energy to treat the dispersion. In the case of periodic systems, this contribution to the energy of cell τ can be expressed as

$$E_{\text{disp}}^{(2)}(\tau) = - \sum_i^{N_{\text{at}}} \sum_{\tau'} \sum_j^{N_{\text{at}}} C_{6,ij}^{\tau\tau'}(\{\mathbf{R}\}) f(R_{ij}^{\tau\tau'}), \quad (1)$$

where τ' is a cell replica index, i and j are indices of atoms in the primitive cell, $C_{6,ij}^{\tau\tau'}(\{\mathbf{R}\})$ is the dispersion coefficient between i in cell τ and j in cell τ' , function in DFT-D3 and DFT-D3(BJ) of the whole set of atomic positions $\{\mathbf{R}\}$, and f is the analytical function used to describe the dispersion which depends on the DFT-D method used, on the chemical

species of i and j , as well as of the distance between the two considered atoms $R_{ij}^{\tau\tau'}$. For example, in DFT-D3 it takes the form

$$f^{\text{D3}}(R_{ij}^{\tau\tau'}) = \frac{1}{2} \left[s_6 \frac{f_{\text{dmp},6}(R_{ij}^{\tau\tau'})}{(R_{ij}^{\tau\tau'})^6} + 3s_8 \sqrt{Q_i} \sqrt{Q_j} \frac{f_{\text{dmp},8}(R_{ij}^{\tau\tau'})}{(R_{ij}^{\tau\tau'})^8} \right], \quad (2)$$

where s_n are coefficients, which depend of the exchange-correlation functional used, $f_{\text{dmp},n}$ are the n th-order damping functions used to remove the short-range divergent behavior of the function, and Q_i are tabulated values expressing the link between lower and higher dispersion coefficients.

As discussed previously, in DFT-D3 and DFT-D3(BJ), the dispersion coefficients depend on the chemical environment around each atom. For sake of brevity, the dependence of this function with respect to the atomic positions $\{\mathbf{R}\}$ will be implied for the remaining of this paper. The dispersion coefficients are interpolated between supporting points as follows:

$$C_{6,ij}^{\tau\tau'} = \frac{1}{L_{ij}^{\text{tot},\tau\tau'}} \sum_{r_i}^{r_i, \text{max}} \sum_{r_j}^{r_j, \text{max}} C_{6,ij,r_i r_j}^{\text{ref}} L_{ij,r_i r_j}^{\tau\tau'}, \quad (3)$$

with r_i the reference for the chemical species of atom i , r_i, max the number of tabulated value available for the considered chemical species (e.g., five in the case of carbon),

$$L_{ij}^{\text{tot},\tau\tau'} = \sum_{r_i}^{r_i, \text{max}} \sum_{r_j}^{r_j, \text{max}} L_{ij,r_i r_j}^{\tau\tau'} \quad (4)$$

and

$$L_{ij,r_i r_j}^{\tau\tau'} = e^{-k_3[(CN_i^{\tau} - CN_{i,r_i}^{\text{ref}})^2 + (CN_j^{\tau'} - CN_{j,r_j}^{\text{ref}})^2]}. \quad (5)$$

The CN_{i,r_i}^{ref} and CN_{j,r_j}^{ref} tensors contain the supporting points for the interpolation, while $C_{6,ij,r_i r_j}^{\text{ref}}$ contains the reference values for the dispersion coefficients, which have been computed beforehand in TDDFT [14]. Finally, $k_3 = 4$ and CN_i^{τ} is the coordination number of atom i in cell τ . In periodic systems, the coordination number as proposed in the original Grimme's paper was a diverging quantity, as pointed out by Reckien [34]. The latter author refined the expression as follows:

$$CN_i^{\tau} = \sum_j^{N_{\text{at}}} \sum_{\tau''} \left[1 + e^{-k_1(k_2 \frac{R_{\text{cov},i} + R_{\text{cov},j}}{R_{ij}^{\tau\tau''}} - 1)} \right]^{-1} f_{\text{dmp},CN}(R_{ij}^{\tau\tau''}), \quad (6)$$

with $R_{\text{cov},i}$ being the covalence radius of species i , $k_1 = 16$, $k_2 = 4/3$ and

$$f_{\text{dmp},CN}(R_{ij}^{\tau\tau''}) = \frac{1}{2} \text{erfc} \left[R_{ij}^{\tau\tau''} - 15k_2(R_{\text{cov},i} + R_{\text{cov},j}) \right]. \quad (7)$$

We use the same expression for our implementation. Note that by translational invariance, all the previous introduced quantities are periodic and thus can be computed taking $\tau = \mathbf{0}$.

In DFT-D3, a three-body correction $E_{\text{disp}}^{(3)}(\tau)$ is also taken into account for the dispersion; it is computed by summing the

partial contribution of all the triplets of atoms

$$E_{\text{disp}}^{(3)}(\boldsymbol{\tau}) = - \sum_i^{N_{\text{at}}} \sum_{\boldsymbol{\tau}'} \sum_j^{N_{\text{at}}} \sum_{\boldsymbol{\tau}''} \sum_k^{N_{\text{at}}} \frac{s_9}{6} C_{9,ijk}^{\boldsymbol{\tau}\boldsymbol{\tau}'\boldsymbol{\tau}''} \times \frac{1 + 3 \cos(\alpha) \cos(\beta) \cos(\gamma)}{(R_{ij}^{\boldsymbol{\tau}\boldsymbol{\tau}'} R_{jk}^{\boldsymbol{\tau}'\boldsymbol{\tau}''} R_{ki}^{\boldsymbol{\tau}''\boldsymbol{\tau}})^3} f_{\text{dmp},9}(\bar{R}_{ijk}^{\boldsymbol{\tau}\boldsymbol{\tau}'\boldsymbol{\tau}''}), \quad (8)$$

where

$$C_{9,ijk}^{\boldsymbol{\tau}\boldsymbol{\tau}'\boldsymbol{\tau}''} = -\sqrt{C_{6,ij}^{\boldsymbol{\tau}\boldsymbol{\tau}'} C_{6,jk}^{\boldsymbol{\tau}'\boldsymbol{\tau}''} C_{6,ki}^{\boldsymbol{\tau}''\boldsymbol{\tau}}}, \quad (9)$$

α, β, γ are the angles of the triangle formed by the triplet of atoms and $f_{\text{dmp},9}$ is the associated damping function with $\bar{R}_{ijk}^{\boldsymbol{\tau}\boldsymbol{\tau}'\boldsymbol{\tau}''}$ the geometrical mean distance between the three atoms of the triplet.

In this work, we will neglect this three-body term (with one exception described later). Indeed, despite arising naturally from the theory of Van der Waals interaction, the use of this three-body term in practical calculations is still debatable, as it tends for example to worsen the cohesive energy for GGA-PBE compared to pairwise corrections alone while improving it for HSE06 [35]. In any case, it yields much smaller contributions to the energy and its derivative than the pairwise term (about 5% of the total dispersion contribution to the binding energy and negligible role on geometry optimization [35]). We nevertheless performed finite differences on this three-body term in order to estimate its contribution to the IFCs. The results are presented in Sec. IV.

For the first-order perturbation (forces and stresses), it is shown in Ref. [33] that the pairwise contribution to forces and stresses scale as $O(N_{\text{at}}^2)$, while the one of the three-body term scales as $O(N_{\text{at}}^3)$ [36].

The pairwise dispersion contribution to the IFCs is given by

$$C_{\kappa\alpha,\kappa'\beta}^{\text{disp}}(\mathbf{0}, \mathbf{b}) = \frac{\partial^2 E_{\text{disp}}}{\partial R_{\kappa\alpha}^0 \partial R_{\kappa'\beta}^b}, \quad (10)$$

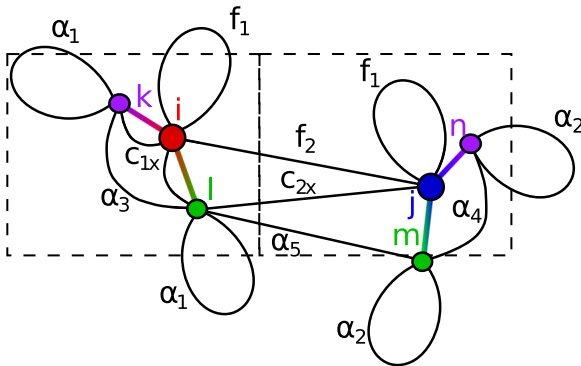


FIG. 1. Schematic representation of the DFT-D contribution to the IFCs detailed in Eq. (11) and in Ref. [33]. There are nine distinct terms labeled f_1, f_2, α_1 to α_5, c_{1x} , and c_{2x} ; i and j refer to the atom considered in the pairwise term. k and l are the atoms that contribute to the coordination number of atom i , while m and n contribute to the coordination of atom j . A plain black line that connects two atoms refers to the second derivative of i - j pair contribution to the dispersion energy with respect to the displacements of these two atoms.

where α, β corresponds to the directions along which the atoms are moved.

From Eq. (1), one can see that the dispersion contribution to IFCs for the pairwise term will be linked to the second derivative of $f(R_{ij}^{\boldsymbol{\tau}\boldsymbol{\tau}'})$, and in the case of DFT-D3 and DFT-D3(BJ), to the second derivative of $C_{6,ij}^{\boldsymbol{\tau}\boldsymbol{\tau}'}$ and to the cross derivatives of $f(R_{ij}^{\boldsymbol{\tau}\boldsymbol{\tau}'})$ and $C_{6,ij}^{\boldsymbol{\tau}\boldsymbol{\tau}'}$ with respect to two atomic displacements. The derivatives of $C_{6,ij}^{\boldsymbol{\tau}\boldsymbol{\tau}'}$ are themselves related to the derivatives of $CN_i^{\boldsymbol{\tau}}$ and $CN_j^{\boldsymbol{\tau}'}$. These dispersion contributions to the IFCs include thus many terms: all of them, as well as which atoms are involved, are shown schematically in Fig. 1.

Mathematically, the full contribution is given by

$$C_{\kappa\alpha,\kappa'\beta}^{\text{disp}}(\mathbf{0}, \mathbf{b}) = \underbrace{C_{\kappa\alpha,\kappa'\beta}^{\text{disp},f1}(\mathbf{0}, \mathbf{b}) + C_{\kappa\alpha,\kappa'\beta}^{\text{disp},f2}(\mathbf{0}, \mathbf{b})}_{f \text{ derivatives}} + \underbrace{C_{\kappa\alpha,\kappa'\beta}^{\text{disp},\alpha1}(\mathbf{0}, \mathbf{b}) + C_{\kappa\alpha,\kappa'\beta}^{\text{disp},\alpha2}(\mathbf{0}, \mathbf{b}) + C_{\kappa\alpha,\kappa'\beta}^{\text{disp},\alpha3}(\mathbf{0}, \mathbf{b})}_{CN_i \& CN_j \text{ derivatives}} + \underbrace{C_{\kappa\alpha,\kappa'\beta}^{\text{disp},\alpha4}(\mathbf{0}, \mathbf{b}) + C_{\kappa\alpha,\kappa'\beta}^{\text{disp},\alpha5}(\mathbf{0}, \mathbf{b})}_{f \times CN_i \& f \times CN_j \text{ derivatives}} + C_{\kappa\alpha,\kappa'\beta}^{\text{disp},c1 \times}(\mathbf{0}, \mathbf{b}) + C_{\kappa\alpha,\kappa'\beta}^{\text{disp},c2 \times}(\mathbf{0}, \mathbf{b}). \quad (11)$$

The discrete Fourier transform of this last expression for a \mathbf{q} vector of the reciprocal space,

$$\tilde{C}_{\kappa\alpha,\kappa'\beta}^{\text{disp}}(\mathbf{q}) = \sum_b C_{\kappa\alpha,\kappa'\beta}^{\text{disp}}(\mathbf{0}, \mathbf{b}) e^{i\mathbf{q} \cdot \mathbf{R}_b}, \quad (12)$$

can be added to the dynamical matrix calculated in DFPT for the computation of the phonon frequencies and eigenmodes of the crystal under study.

The full theoretical derivation of this last Fourier transform can be found in Ref. [33]. It will be shown that, for the pairwise term, the DFT-D contribution to the dynamical matrix scales only as $O(N_{\text{at}}^3)$.

To validate these expressions, frozen-phonon computations were realized and are presented in Sec. III. This theoretical framework was then applied on specific materials to compute their phonon frequencies with inclusion of DFT-D contributions; the results are presented and discussed in Sec. IV.

III. IMPLEMENTATION AND TESTS

DFT-D methods have been implemented within the ABINIT software [22,37] for both ground-state and for atomic response functions. As the previously introduced contributions to the energy, forces, stresses, and interatomic force constants can not be computed for an infinite number of cell replica, a tolerance is used to define the number of cells to be considered in the DFT-D correction. For the computation of the coordination number, the cutoff radius was set to 106 \AA , while for the pairwise term, a tolerance on the energy of 10^{-12} Ha is used [38].

First, our implementation has been validated with respect to Grimme's code [39]. We tested graphite (AB stacking) with the GGA-PBE functional and with the in-plane and out-plane lattice parameters used as the relaxed DFT-D3 ones,

TABLE I. Validation of our implementation by comparison of dispersion contribution to IFCs (reduced coordinates) in DFT-D3 computed by frozen phonons and by DFPT. The q vector is given in reduced coordinates.

	Frozen phonons DFT-D IFCs (mHa)	DFPT DFT-D IFCs (mHa)
$\Re[\tilde{C}_{1313}^{\text{disp}}(\Gamma)]$	−10.975002073	−10.975002080
$\Re[\tilde{C}_{1313}^{\text{disp}}(\mathbf{A})]$	−16.681563853	−16.681563203
$\Re[\tilde{C}_{1313}^{\text{disp}}(0,0,1/3)]$	−15.310251633	−15.310251646
$\Re[\tilde{C}_{1323}^{\text{disp}}(0,0,1/3)]$	13.009670591	13.009670637
$\Im[\tilde{C}_{1323}^{\text{disp}}(0,0,1/3)]$	0.000000000	0.000000000

i.e., 2.46 and 6.96 Å. The computation with ABINIT of the pairwise and three-body dispersion energies gave, respectively, −13.40 and 1.286 mHa for DFT-D3. These values have to be compared to −13.42 and 1.284 mHa obtained with Grimme’s code. For DFT-D 2 and DFT-D3(BJ), we obtain for the pairwise term −16.826 and −22.00 mHa in ABINIT, respectively, while we get −16.824 and −22.03 mHa with Grimme’s code. The remaining discrepancies for DFT-D3 and DFT-D3(BJ) can be explained by the absence of a cutoff for the coordination number in Grimme’s code, while present in our implementation. These tests validate the implementation of these DFT-D methods inside the ABINIT software.

Second, in order to validate the dispersion contribution to the IFCs in reciprocal space, we computed this quantity with DFPT and frozen phonons at specific q points using supercells. We used relative atomic displacements of 10^{-7} and a first-order finite difference technique on the forces to get these values.

The comparison for graphite of the DFT-D3 contribution to the IFCs with our implementation and with finite difference is illustrated in Table I, with the three-body term being neglected in the two cases. As one can see, agreement up to six digits can be easily achieved. This confirms the validity of the previously introduced mathematical derivations.

Finally, we examined the influence on the IFCs of the three-body term, if included, compared to the one of the pairwise term thanks to the same finite difference technique. The energy tolerance was set for this three-body term to 10^{-11} Ha and computations were performed at the DFT-D3 (pairwise only) geometry of graphite. We obtained for the specific three-body contribution $\tilde{C}_{1313}^{3\text{-bt}}(\Gamma) \approx -1.6$ mHa, around 15% of the pairwise contribution to the IFCs (equal to −10.975 mHa in our case). In consequence, neglecting this three-body contribution to the IFCs is an approximation with an impact similar to neglecting it at the total energy or geometry relaxation levels (that we do anyway in this paper).

IV. APPLICATIONS

In this section, we present some results obtained with our implementation. We took three well-known materials that require dispersion corrections to be properly described with an *ab initio* method: solid argon, graphite, and benzene. All computations are performed in DFT/DFPT and with the software ABINIT.

The GGA-PBE approximation [40] was adopted for the exchange-correlation functional in addition of the DFT-D methods. As already mentioned, we neglect the three-body contribution for ground-state and vibrational properties. An energy cutoff smearing [41] of 0.5 Ha is used and geometry optimizations were carried on until the forces on each atom were smaller than 10^{-8} Ha/Bohr. Phonon frequencies were computed at relaxed lattice parameters. We use such strict relaxation criterion due to the weak nature of the dispersive forces. Concerning the convergence criteria with respect to the plane-wave cutoff energy and to the density of the Monkhorst grid [42], we required a precision better than 0.2% on the lattice parameters and of 1 cm^{-1} on the low-frequency modes, referred as “lattice” modes in this paper. Further computational details, like convergence parameters for each material under study, are given in the Ref. [33].

We use the following definition for the cohesive energy per unit cell of the crystal:

$$E_{\text{coh}} = \frac{E_{\text{solid}}}{N} - E_{\text{gas}}, \quad (13)$$

where E_{solid} is the total energy computed at the relaxed position, E_{gas} is the total energy computed when the atoms, layers, or molecules are at least 16 Å away from their closest neighbor, and N is the number of molecules per primitive cell in the crystal. It is finally important to mention that we neglect the effect of the zero-point motion on the cohesive energy, equilibrium lattice parameters, and phonon frequencies in our computation, although anharmonic effects may play an important role in molecular crystals.

A. Argon

The isotope 36 of argon crystallizes in the FCC spatial arrangement at around 84 K under normal conditions. Due to the dispersive nature of the long-range interactions between the Ar atoms, DFT-PBE fails to describe properly this system: it predicts a lattice constant of 5.95 Å, quite off compared to the experimental value of 5.30017 Å [43] at 4.25 K. DFT-D2, -D3, and -D3(BJ) give 5.37, 5.56, and 5.48 Å for the lattice parameter, respectively, in better agreement with the experiments. Our DFT-D3(BJ) implementation gives a cohesive energy of −88 meV, consistent with the value of −87 meV reported in the literature with the same method in VASP [35].

The phonon band structures of Ar computed with the different DFT-D methods are presented in Fig. 2. In each case, the computations were performed at the corresponding relaxed lattice parameters and imposing the mass of the argon as 36 amu. Experimental measurements performed at 10 K by Fujii and coworkers [44] are also shown.

At first sight, one can see that DFT-PBE, without vdW corrections, lies quite far from the experimental data. Better agreement is achieved with DFT-D contributions, especially DFT-D2. The upper branch of the spectrum is particularly well reproduced in this last method. It has to be noticed that the dispersion is quite remarkably similar with all the methods; the frequencies are just underestimated, for example, in DFT-PBE by an almost constant factor. The better agreement with the experimental data of the DFT-D2 results, compared with

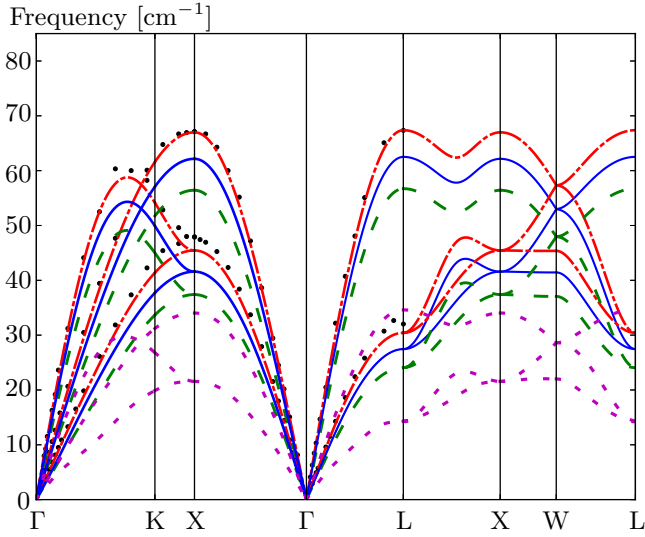


FIG. 2. Phonon band structure of solid ^{36}Ar computed with the different DFT-D corrections at the corresponding relaxed lattice parameter. Dotted purple: DFT-PBE without DFT-D correction. Dashed green: DFT-D3. Solid blue: DFT-D3(BJ). Dash-dot red: DFT-D2. In each case, the computations were performed at the corresponding relaxed lattice parameters. Experimental data from Ref. [44] are also shown (black dots).

DFT-D3 or DFT-D3(BJ), is primarily due to its better lattice constant.

Finally, we computed the phonon band structure at the experimental lattice constant 5.30017 \AA [43] to get further insights on the direct effect of the DFT-D methods on the phonon frequencies. Indeed, these methods give a quite different lattice parameter for argon. The results are shown in Fig. 3.

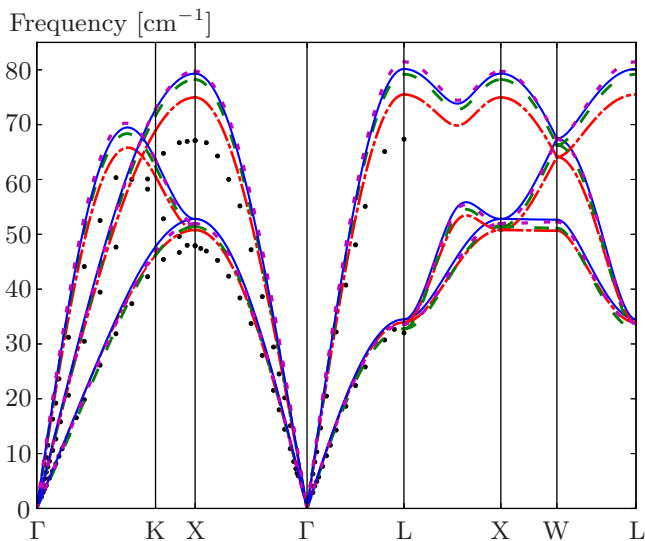


FIG. 3. Phonon band structure of solid ^{36}Ar computed with the different DFT-D corrections at the experimental lattice parameter. Dotted purple: DFT-PBE without DFT-D correction. Dashed green: DFT-D3. Solid blue: DFT-D3(BJ). Dash-dot red: DFT-D2. Experimental data from Ref. [44] are also shown (black dots).

TABLE II. Lattice parameters and graphite cohesive energy per carbon atom computed with the different DFT-D methods. Results obtained by Hazrati, Sabatini, and their respective co-workers with the family of vdW-DF methods [25,46], as well as experimental data are also shown.

Correction	a (\AA)	d (\AA)	E_{coh} (meV/C)
DFT-PBE	2.46	4.4	-1.3
DFT-D2	2.45	3.21	-57.8
DFT-D3	2.46	3.48	-48.9
DFT-D3(BJ)	2.46	3.37	-53.9
optB88-vdW ^a	2.47	3.36	-69.5
vdW-DF2 ^b	2.47	3.52	
rVV10 ^b	2.46	3.36	
Exp.	2.4589 ^c	3.3538 ^c	$-52 \pm 5^{\text{d}}$

^aReference [46].

^bReference [25], Table 6-1.

^cReference [45].

^dReference [47].

One can see that in all the cases, the phonon band structures overestimate the experimental results. It seems once again that DFT-D2 improves the agreement with the experiments while DFT-D3 and DFT-D3(BJ) lies quite close to the DFT-PBE phonon band structure. Further discussions on the importance of the contribution to the IFCs of the DFT-D corrections can be found in Ref. [33].

B. Graphite

In graphite, each layer is bound to the neighboring ones by weak forces. Therefore this material requires proper description of these interactions in DFT. We focus in this work on AB-stacked graphite.

The interlayer distance predicted in PBE (4.4 \AA) largely overestimates the experimental value of 3.34 \AA [45]. The use of DFT-D2 gives an interlayer distance of 3.21 \AA and thus tends to overestimate the binding force between the layers. DFT-D3 and DFT-D3(BJ) predict 3.48 and 3.37 \AA distances, respectively, within 4% and 1% of the experiments, respectively. The values of the in-plane lattice parameter and cohesive energy can be found in Table II.

The graphite lattice phonon bands along Γ -A, with the different methods, are shown in Fig. 4. For an easier comparison, the lattice phonon frequencies at Γ and A are reported in Table III alongside with experimental data (at room temperature) and results obtained with vdW-DF2 (and other optimized functionals for the vdW).

As one can see, the lattice modes are underestimated in DFT-PBE (largely) and in DFT-D3 with respect to experiments. DFT-D2 describes much better the Γ_{LO} but overestimates by more than 20 cm^{-1} the Γ_{ZO} mode. DFT-D3(BJ) works better to describe the higher lattice branch—although being as poor as the other methods for the Γ_{LO} one—and yields similar precision with the more sophisticated vdW-DF2 methods (and other optimized functionals for the vdW) to describe these lattice modes. These discrepancies may be explained by the choice of the exchange-correlation

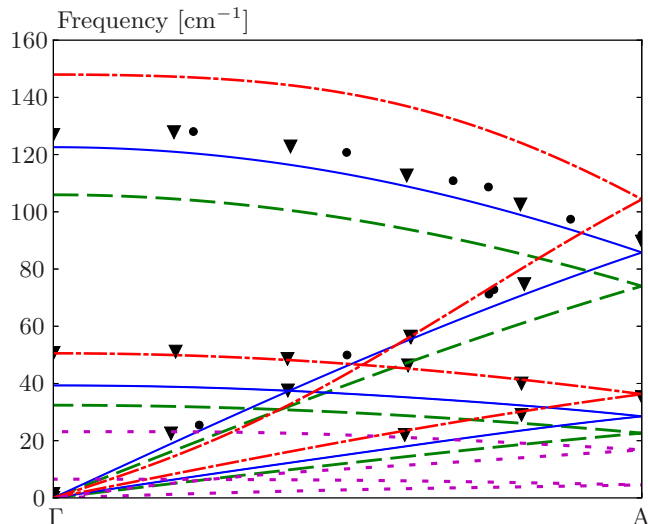


FIG. 4. Phonon band structure of low-frequency modes of graphite computed with DFT-PBE as well as adding to it different DFT-D corrections. Dotted purple: computed without DFT-D corrections. Dash-dot red: computed with DFT-D2. Dashed green: computed with DFT-D3. Solid blue: computed with DFT-D3(BJ). In each case, the computations were performed at the corresponding relaxed lattice parameters. Experimental data from Ref. [48] (black dots) and Ref. [49] (black triangles) are also shown.

approximation but perhaps as well by temperature effects (experimental data are performed at room temperature).

In addition, we computed at experimental lattice constants [45] the phonon branches along Γ -A with the different DFT-D methods. The results are shown in Fig. 5.

DFT-PBE and DFT-D3 give quite similar results while DFT-D3(BJ) lies closer to the experiments for the high-frequency lattice branch. DFT-D2 is completely off, predicting negative phonon frequencies, which typically indicates a phase instability. These negative phonon modes have likely the same

TABLE III. Low phonon frequencies of graphite computed with different methods to treat the dispersion and at special points of the reciprocal space. Results obtained by Hazrati and co-workers with optB88-vdW [46], by Sabatini [25] are also presented as well as experimental data from Nicklow and co-workers [49].

Frequencies	Γ_{LO}	Γ_{ZO}	$A_{TA/TO}$	$A_{LA/LO}$
DFT-PBE	6.5	23	4.5	17
DFT-D2	51	148	36	104
DFT-D3	32	106	23	74
DFT-D3(BJ)	39	123	29	86
optB88-vdW ^a	40	139	28	95
rVV10 ^b	41	140	29	98
vdW-DF2 ^b	31	118	22	82
Exp. ^c	49	126	35	89
Exp. ^d	42	127		

^aReference [46].

^bReference [25], Fig. 6-3.

^cReference [48], Fig. 4.

^dReference [48], p. 2.

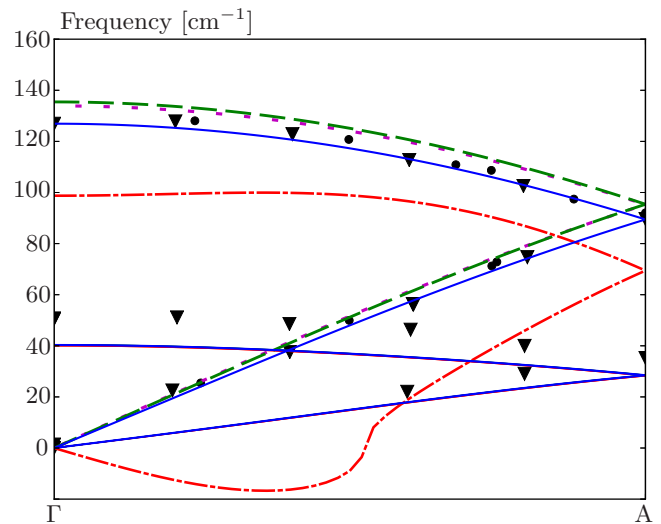


FIG. 5. Phonon band structure of low-frequency modes of graphite computed for different methods on top of PBE at experimental lattice parameters [45]. Dotted purple: computed without DFT-D corrections. Dash-dot red: computed with DFT-D2. Green: computed with DFT-D3. Solid blue: computed with DFT-D3(BJ). Experimental data from Ref. [48] (black dots) and Ref. [49] (black triangles) are also shown.

origin with the underestimation in DFT-D2 of the out-of-plane lattice constant compared to the experiments.

C. Benzene

Finally, we studied the benzene molecular crystal. This material crystallizes at 5.5 °C; its primitive cell is orthorhombic (Pbca space group) and contains four C_6H_6 molecules.

With DFT-PBE, we observed a large overestimation of the experimental volume [50] by more than 30%. This can be explained by the fact that the benzene molecules are bound by vdW interactions in the crystal, which are not included—or somehow spuriously—in PBE. So, it was not meaningful to compute the phonon frequencies in this case. In contrast, relaxations performed with the different DFT-D methods yield a meaningful global energy minimum; the lattice parameters obtained with each method are given in Table IV, as well as their corresponding cohesive energy for the benzene crystal. In this table, we report also the low-temperature experimental data (77 K) $a = 7.292$ Å, $b = 9.471$ Å, and $c = 6.742$ Å [50] and experimental measurements performed by Jeffrey and co-workers at 10 K on deuterated benzene [51] $a = 7.360$ Å, $b = 9.375$ Å, and $c = 6.703$ Å. Concerning the cohesive energy, an estimate of the lattice energy at 0 K [52] of -55.3 ± 2.2 kJ/mol is also shown.

As one can see, DFT-D3 and DFT-D3(BJ) improve markedly the agreement with the experiments, with the later method providing the better description of benzene molecular crystal. Our DFT-D3(BJ) implementation predicts a cohesive energy of -55.0 kJ/mol in agreement both with the theoretical value of -55.0 kJ/mol reported with the same method [35] and with the estimate of the lattice energy at 0 K. In the case of DFT-D2, the results are more contrasted, with the b and c lattice parameters being quite underestimated in this method.

TABLE IV. Benzene lattice parameters and cohesive energy computed with the different DFT-D methods. Available experimental data for the lattice parameters and an estimated value of the lattice energy at 0 K are also reported.

Correction	a (Å)	b (Å)	c (Å)	E_{coh} (kJ/mol)
DFT-D2	7.13	9.07	6.44	-56.3
DFT-D3	7.42	9.48	6.85	-47.4
DFT-D3(BJ)	7.30	9.31	6.70	-55.0
Exp. ^a	7.292	9.471	6.742	
Exp. ^b	7.360	9.375	6.703	
Est. ^c				-55.3 ± 2.2

^aReference [50].

^bReference [51].

^cReference [52].

These discrepancies probably originate from the absence of any dependence of the dispersion coefficient on the close chemical environment around each atom in this method.

As there are three translational and rotational degrees of freedom for each molecule, there are in total 24 lattice modes, including the three acoustic modes. The computed lattice frequencies of benzene at the zone center are reported in Table V alongside with experimental Raman measurements performed at 7 K [53].

As one can see, DFT-D3(BJ) is able to reproduce quite well the experimental frequencies of the lattice modes. On average, the difference is less than 5 cm^{-1} compared to the experiments which is quite acceptable from this degree of theory. Only the B_{1g} mode with 107.3 cm^{-1} experimental frequency, which corresponds to a rotation of the phenyl groups in opposite phases, is relatively poorly described. The discrepancies may

TABLE V. Lattice phonon frequencies of benzene molecular crystal computed at the zone-center wave vector with PBE-D2, PBE-D3, and PBE-D3(BJ). Experimental data from Pinan and co-workers [53] are also presented for Raman active modes, as well as mean average error (MAE) and mean average percentage error (MAPE) for each given method with respect to the experiments.

Sym.	Frequencies				Sym.	Frequencies		
	-D2	-D3	-BJ	Exp. ^a		-D2	-D3	-BJ
A_g	78	54	60	63.3	B_{2u}	75	52	59
B_{1g}	81	60	69	67.0	A_u	68	52	60
B_{3g}	86	55	64	68.7	B_{1u}	88	62	71
B_{2g}	99	75	88	84.9	A_u	89	62	72
A_g	99	74	83	85.0	B_{3u}	89	67	76
B_{2g}	118	82	93	89.4	B_{3u}	110	80	91
B_{2g}	132	94	109	97.3	A_u	121	89	103
A_g	118	84	97	100.6	B_{1u}	124	90	104
B_{3g}	120	88	103	100.6	B_{2u}	125	93	107
B_{1g}	107	77	88	107.3				
B_{1g}	160	120	136	135.0				
B_{3g}	157	119	136	136.0				
MAE (cm^{-1})	18.5	12.7	4.54					
MAPE (%)	20.2	13.4	4.9					

^aReference [53].

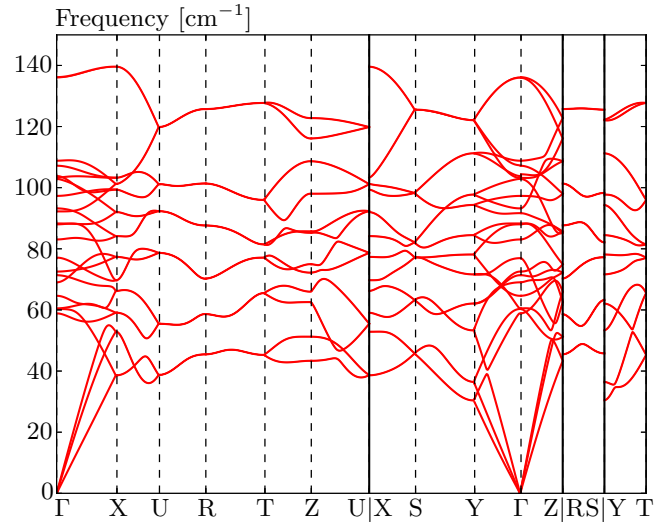


FIG. 6. Lattice phonon band structure of benzene molecular crystal ($Pbca$ space group) computed with PBE-D3(BJ).

arise from several sources: they may come from the choice of the functional approximation (including the vdW method), from the choice of pseudopotentials or from anharmonicity effects. We also observed only weak LO-TO splitting for the lattice modes; the most important effect in DFT-D3(BJ) is seen for the B_{1u} at 103 cm^{-1} that is shifted by 0.6 cm^{-1} upwards for a nonanalyticity alongside c^* axis.

In addition, we computed the phonon band structure and phonon density of states of this material with DFT-D3(BJ). The phonon band structure and the phonon DOS for the lattice modes are presented in Figs. 6 and 7, respectively. As one can see in Fig. 6, the 24 lattice modes merge into six modes along U-R, R-T, and R-S branches. We observe that the phonon

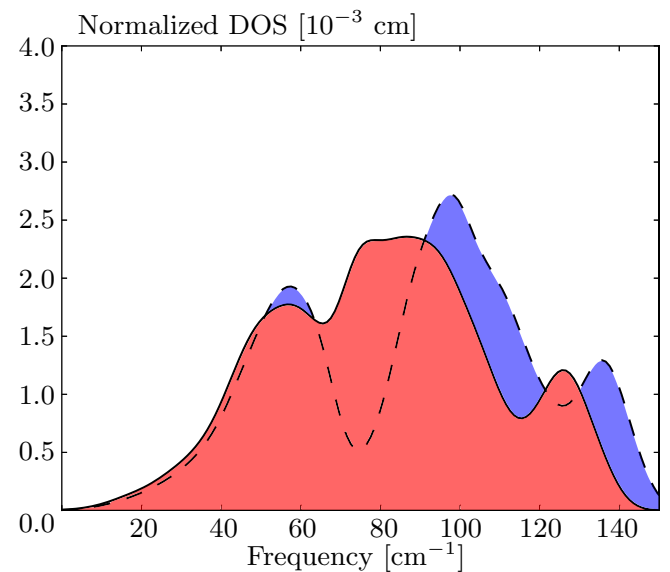


FIG. 7. Comparison between the lattice phonon density of states of benzene molecular crystal computed with DFT-D3(BJ) at the experimental lattice parameters [51] (blue-filled dotted line) and at the DFT-D3(BJ) relaxed ones (plain curve filled with red).

density of states computed at relaxed DFT-D3(BJ) has the following peak maxima: 57, 78, 87, and 126 cm^{-1} , which are in reasonable agreement with the experimental peaks reported by Pinan and coworkers in the double-resonance Raman spectrum [53], i.e., at around 40, 80, 90, and 120 cm^{-1} . It has to be noticed, though, that the discrepancies may arise from anharmonic effects, present in the experiments but that we neglect in our computation. An additional graph presented in Ref. [33], Fig. S2, compares the phonon density of states computed at DFT-D3(BJ), with and without the DFT-D3(BJ) correction.

Finally, the lattice phonon density of states computed at experimental lattice parameters and internal positions [51] with DFT-D3(BJ) is also shown in Fig. 7. As one can see, working at experimental parameters does not improve globally the agreement with the experiments, as only three peaks are observed in that case, in contradiction with the experiments.

V. CONCLUSION

We have presented in this work the theoretical derivation of the pairwise part of the DFT-D contribution to the IFCs and dynamical matrices, as well as its implementation inside the ABINIT software. We have validated the implementation with respect to frozen-phonon computations, and also tested the hypothesis that the contribution from three-body interactions can be neglected. We have then applied this new implementation to the computation of the phonon band structures of argon, graphite, and benzene materials, which are known to require proper description of the long-range e^-e^- correlation. We have analyzed the specific role of the correctness of the equilibrium parameters, and the one of the direct modification of dynamical matrices by the DFT-D contribution.

For argon, all the DFT-D methods improve markedly over the DFT-PBE results. An excellent agreement with experimental data is even obtained for the DFT-D2 method, taken at its relaxed lattice parameter. The agreement for the DFT-D3 and DFT-D3(BJ), again at their relaxed lattice parameter is less satisfactory, but still within 10%–20% of the experiment. If one works at the experimental equilibrium lattice parameter, all DFT-D (or DFT-PBE) methods overestimate the phonon frequencies, by a few percent, the best agreement being again obtained with DFT-D2.

For graphite, at the corresponding relaxed lattice parameters, all DFT-D methods also improve enormously with respect to DFT-PBE for the description of the low-lying bands, the

DFT-D3(BJ) or the DFT-D2 being the best, depending on the considered branch. The agreement is again still within 10%–20% of the experiment for these low-lying bands, for all DFT-D methods. When fixing the lattice parameter at the experimental value, DFT-PBE, DFT-D3, and DFT-D3(BJ) methods give very similar results, while DFT-D2 is considerably off, and even predict instabilities of the lattice.

For benzene, for the 12 low-lying modes at Γ for which experimental data (Raman) are available, spanning the range between 63.3 and 163 cm^{-1} , the DFT-D3(BJ) has a maximum discrepancy of 19.2 cm^{-1} , while ten modes are obtained within 5 cm^{-1} of the experimental values. The performance of the DFT-D3 method is less satisfactory, but still reasonable.

Globally, these dispersive contributions to the IFCs can not be neglected and are important to properly reproduce experimental results. Overall, the DFT-D3(BJ) is the most reliable method from what we observed.

This work opens the way for the computation of more advanced response properties of molecular crystals in DFPT, like Raman spectra, the temperature dependence of electronic properties within the Allen-Heine-Cardona formalism [54–60], or thermodynamic properties within the quasiharmonic approximation [61–65]. Further developments may include the derivation of strain perturbation for the DFT-D methods, as well as the developments of dispersive contributions beyond pairwise-additive models [66], which should describe in a more adequate way the many-body nature of the vdW interactions.

ACKNOWLEDGMENTS

The authors acknowledge technical help from J.-M. Beuken and M. Giantomassi. This work was supported by the FRS-FNRS through a FRIA Grant (B.V.T.) and by the Communauté française de Belgique through the BATTAB project (ARC 14/19-057). Computational resources have been provided by the supercomputing facilities of the Université catholique de Louvain (CISM/UCL) and the Consortium des Equipements de Calcul Intensif en Fédération Wallonie Bruxelles (CECI) funded by the Fonds de la Recherche Scientifique de Belgique (FRS-FNRS) under convention 2.5020.11. The present research benefited from computational resources made available on the Tier-1 supercomputer of the Fédération Wallonie-Bruxelles, infrastructure funded by the Walloon Region under the Grant Agreement No. 1117545.

-
- [1] R. Martin, *Electronic Structure, Basic Theory and Practical Methods* (Cambridge University Press, Cambridge, UK, 2004).
 - [2] J. Klimeš and A. Michaelides, *J. Chem. Phys.* **137**, 120901 (2012).
 - [3] A. Tkatchenko and M. Scheffler, *Phys. Rev. Lett.* **102**, 073005 (2009).
 - [4] H. Rydberg, M. Dion, N. Jacobson, E. Schroder, P. Hyldgaard, S. I. Simak, D. C. Langreth, and B. I. Lundqvist, *Phys. Rev. Lett.* **91**, 126402 (2003).
 - [5] M. Dion, H. Rydberg, E. Schroder, D. C. Langreth, and B. I. Lundqvist, *Phys. Rev. Lett.* **92**, 246401 (2004).
 - [6] K. Lee, Éamonn D. Murray, L. Kong, B. I. Lundqvist, and D. C. Langreth, *Phys. Rev. B* **82**, 081101 (2010).
 - [7] P. L. Silvestrelli, *Phys. Rev. Lett.* **100**, 053002 (2008).
 - [8] A. Ambrosetti and P. L. Silvestrelli, *Phys. Rev. B* **85**, 073101 (2012).
 - [9] F. Furche, *Phys. Rev. B* **64**, 195120 (2001).
 - [10] M. Fuchs and X. Gonze, *Phys. Rev. B* **65**, 235109 (2002).
 - [11] X. Ren, P. Rinke, C. Joas, and M. Scheffler, *J. Mater. Sci.* **47**, 7447 (2012).
 - [12] D. Lu, Y. Li, D. Rocca, and G. Galli, *Phys. Rev. Lett.* **102**, 206411 (2009).

- [13] S. Grimme, *J. Comput. Chem.* **27**, 1787 (2006).
- [14] S. Grimme, J. Anthony, S. Ehrlich, and H. Krieg, *J. Chem. Phys.* **132**, 154104 (2010).
- [15] S. Grimme, S. Ehrlich, and L. Goerigk, *J. Comput. Chem.* **32**, 1456 (2010), this paper proposes the adaptation to Ref. [14] of a damping, following the idea of Becke and Johnson [67].
- [16] V. V. Gobre and A. Tkatchenko, *Nat. Commun.* **4**, 2341 (2013).
- [17] B. M. Axilrod and E. Teller, *J. Chem. Phys.* **11**, 299 (1943).
- [18] J. Muto, *Proc. Phys. Math. Soc. Jpn.* **17**, 629 (1943).
- [19] P. Giannozzi, S. de Gironcoli, P. Pavone, and S. Baroni, *Phys. Rev. B* **43**, 7231 (1991).
- [20] X. Gonze, *Phys. Rev. B* **55**, 10337 (1997).
- [21] X. Gonze and C. Lee, *Phys. Rev. B* **55**, 10355 (1997).
- [22] X. Gonze, G.-M. Rignanese, M. Verstraete, J.-M. Beuken, Y. Pouillon, R. Caracas, F. Jollet, M. Torrent, G. Zerah, M. Mikami, P. Ghosez, M. Veithen, J.-Y. Raty, V. Olevano, F. Bruneval, L. Reining, R. Godby, G. Onida, D. R. Hamann, and D. C. Allan, *Z. Kristallogr.* **220**, 558 (2005).
- [23] D. R. Hamann, K. M. Rabe, and D. Vanderbilt, *Phys. Rev. B* **72**, 033102 (2005).
- [24] X. Wu, D. Vanderbilt, and D. R. Hamann, *Phys. Rev. B* **72**, 035105 (2005).
- [25] R. Sabatini, Non-local correlation in Density Functional Theory, Ph.D. thesis, Scuola Internazionale Superiore di Studi Avanzati, 2012.
- [26] J. D. Gale, *J. Chem. Soc., Faraday Trans.* **93**, 629 (1997).
- [27] H. Fang, M. T. Dove, and K. Refson, *Phys. Rev. B* **90**, 054302 (2014).
- [28] A. O. de-la Roza and E. R. Johnson, *J. Chem. Phys.* **137**, 054103 (2012).
- [29] A. M. Reilly and A. Tkatchenko, *J. Chem. Phys.* **139**, 024705 (2013).
- [30] A. M. Reilly and A. Tkatchenko, *Phys. Rev. Lett.* **113**, 055701 (2014).
- [31] I. Fedorov, F. Marsusi, T. Fedorova, and Y. Zhuravlev, *J. Phys. Chem. Solids* **83**, 24 (2015).
- [32] X. Ling, L. Liang, S. Huang, A. A. Puzdov, D. B. Geohegan, B. G. Sumpter, J. Kong, V. Meunier, and M. S. Dresselhaus, *Nano Lett.* **15**, 4080 (2015).
- [33] See Supplemental Material at <http://link.aps.org/supplemental/10.1103/PhysRevB.93.144304> for the theoretical derivation of the dispersion contribution to the IFCs, additional graphs on their importance in practice, as well as computational details.
- [34] W. Reckien, F. Janetzko, M. F. Peintinger, and T. Bredow, *J. Comput. Chem.* **33**, 2023 (2012).
- [35] J. Moellmann and S. Grimme, *J. Phys. Chem. C* **118**, 7615 (2014).
- [36] It is already the case in Grimme's software, www.thch.uni-bonn.de/tc/index.php.
- [37] X. Gonze, B. Amadon, P.-M. Anglade, J.-M. Beuken, F. Bottin, P. Boulanger, F. Bruneval, D. Caliste, R. Caracas, M. Côté, T. Deutsch, L. Genovese, P. Ghosez, M. Giantomassi, S. Goedecker, D. Hamann, P. Hermet, F. Jollet, G. Jomard, S. Leroux, M. Mancini, S. Mazevet, M. Oliveira, G. Onida, Y. Pouillon, T. Rangel, G.-M. Rignanese, D. Sangalli, R. Shaltaf, M. Torrent, M. Verstraete, G. Zerah, and J. Zwanziger, *Comput. Phys. Commun.* **180**, 2582 (2009).
- [38] Only the pairs for which the contribution to DFT-D energy is higher than the tolerance are considered.
- [39] www.thch.uni-bonn.de/tc/index.php.
- [40] J. P. Perdew, K. Burke, and M. Ernzerhof, *Phys. Rev. Lett.* **77**, 3865 (1996).
- [41] M. Bernasconi, G. Chiarotti, P. Focher, S. S. E. Tosatti, and M. Parrinello, *J. Phys. Chem. Solids* **56**, 501 (1995).
- [42] H. J. Monkhorst and J. D. Pack, *Phys. Rev. B* **13**, 5188 (1976).
- [43] O. G. Peterson, D. N. Batchelder, and R. Simmons, *Phys. Rev.* **150**, 703 (1966).
- [44] Y. Fujii, N. Lurie, R. Pynn, and G. Shirane, *Phys. Rev. B* **10**, 3647 (1974).
- [45] Y. Baskin and L. Meyer, *Phys. Rev.* **100**, 544 (1955).
- [46] E. Hazrati, G. A. de Wijs, and G. Brocks, *Phys. Rev. B* **90**, 155448 (2014).
- [47] R. Zacharia, H. Ulbricht, and T. Hertel, *Phys. Rev. B* **69**, 155406 (2004).
- [48] M. Mohr, J. Maultzsch, E. Dobardzic, S. Reich, I. Milosevic, M. Damjanovic, A. Bosak, M. Krisch, and C. Thomsen, *Phys. Rev. B* **76**, 035439 (2007).
- [49] R. Nicklow, N. Wakabayashi, and H. G. Smith, *Phys. Rev. B* **5**, 4951 (1972).
- [50] V. M. Kohzin, *Zh. Fiz. Khim.* **28**, 566 (1954).
- [51] G. A. Jeffrey, J. R. Ruble, R. McMullan, and J. A. Pople, *Proc. R. Soc. London A* **414**, 597 (1987).
- [52] J. Yang, W. Hu, D. Usvyat, D. Matthews, M. Schütz, and G. K.-L. Chan, *Science* **345**, 640 (2014).
- [53] J. Pinan, R. Ouillon, P. Ranson, M. Becussi, and S. Califano, *J. Chem. Phys.* **109**, 5469 (1998).
- [54] P. B. Allen and M. Cardona, *Phys. Rev. B* **27**, 4760 (1983).
- [55] X. Gonze, P. Boulanger, and M. Côté, *Ann. Phys. (Berlin)* **523**, 168 (2011).
- [56] S. Poncé, G. Antonius, P. Boulanger, E. Cannuccia, A. Marini, M. Côté, and X. Gonze, *Comput. Mater. Sci.* **83**, 341 (2014).
- [57] S. Poncé, G. Antonius, Y. Gillet, P. Boulanger, J. Laflamme Janssen, A. Marini, M. Côté, and X. Gonze, *Phys. Rev. B* **90**, 214304 (2014).
- [58] S. Poncé, Y. Gillet, J. Laflamme Janssen, A. Marini, M. Verstraete, and X. Gonze, *J. Phys. Chem.* **143**, 102813 (2015).
- [59] G. Antonius, S. Poncé, P. Boulanger, M. Côté, and X. Gonze, *Phys. Rev. Lett.* **112**, 215501 (2014).
- [60] G. Antonius, S. Poncé, E. Lantagne-Hurtubise, G. Auclair, X. Gonze, and M. Côté, *Phys. Rev. B* **92**, 085137 (2015).
- [61] M. Born and K. Huang, *Dynamical Theory of Crystal Lattices* (Oxford University Press, New York, 1988).
- [62] G.-M. Rignanese, J.-P. Michenaud, and X. Gonze, *Phys. Rev. B* **53**, 4488 (1996).
- [63] A. I. Lichtenstein, R.O. Jones, S. de Gironcoli, and S. Baroni, *Phys. Rev. B* **62**, 11487 (2000).
- [64] M. Lazzeri and S. de Gironcoli, *Phys. Rev. B* **65**, 245402 (2002).
- [65] P. Carrier, J. F. Justo, and R. M. Wentzcovitch, *Phys. Rev. B* **78**, 144302 (2008).
- [66] A. M. Reilly and A. Tkatchenko, *Chem. Sci.* **6**, 3289 (2015).
- [67] E. R. Johnson and A. D. Becke, *J. Chem. Phys.* **124**, 174104 (2006).